HHS Public Access

Author manuscript

Exp Eye Res. Author manuscript; available in PMC 2023 March 01.

Published in final edited form as:

Exp Eye Res. 2022 March ; 216: 108933. doi:10.1016/j.exer.2022.108933.

Decorin Regulates Collagen Fibrillogenesis During Corneal Wound Healing in Mouse *in vivo*

Suneel Gupta[a,b], **Filiz Buyank**[c], **Nihant R. Sinha**[a,b], **DeAna G. Grant**[d], **Prashant R. Sinha**[a,b], **Renato V. Iozzo**[e], **Shyam S. Chaurasia**[a,b,+], **Rajiv R. Mohan**[a,b,f,*]

[a]Harry S. Truman Memorial Veterans' Hospital, Columbia, Missouri, USA.

[b]Departments of Veterinary Medicine & Surgery and Biomedical Sciences, College of Veterinary Medicine, University of Missouri, Columbia, Missouri, USA.

[c]Department of Computer Science, University of Missouri, Columbia, Missouri, USA.

[d]Electron Microscopy Core, University of Missouri, Columbia, Missouri, USA.

[e]Department of Pathology, Anatomy, and Cell Biology, and Translational Cellular Oncology Program, Thomas Jefferson University, Philadelphia, Pennsylvania, USA.

[f]Mason Eye Institute, School of Medicine, University of Missouri, Columbia, Missouri, USA.

Abstract

A characteristic rigid spatial arrangement of collagen fibrils in the stroma is critical for corneal transparency. This unique organization of collagen fibrils in corneal stroma can be impacted by the presence and interactions of proteoglycans and extracellular matrix (ECM) proteins in a corneal microenvironment. Earlier studies revealed that decorin, a leucine-rich proteoglycan in stroma, regulates keratocyte-collagen matrix assembly and wound healing in the cornea. This study investigated the role of decorin in the regulation of stromal fibrillogenesis and corneal transparency *in vivo* employing a loss-of-function genetic approach using decorin null ($dcn^{-/-}$) and wild type ($dcn^{+/+}$) mice and a standard alkali-injury model. A time-dependent ocular examinations with Slit lamp microscope in live animals assessed corneal clarity, haze, and neovascularization levels in normal and injured eyes. Morphometric changes in normal and injured $dcn^{+/+}$ and $dcn^{-/-}$ corneas, post-euthanasia, were analyzed with Masson's Trichrome and Periodic Acid-Schiff (PAS) histology evaluations. The ultrastructure changes in all corneas were investigated with transmission electron microscopy (TEM). Injury to eye produced clinically relevant corneal haze and neovascularization in $dcn^{-/-}$ and $dcn^{+/+}$ mice while corneas of uninjured eyes remained clear and avascular. A clinically significant haze and neovascularization appeared in injured $dcn^{-/-}$ corneas compared to the $dcn^{+/+}$ corneas at day 21 post-injury and not at

[*]**Corresponding author**: Rajiv R. Mohan, MS, PhD, FARVO, Professor of Ophthalmology & Molecular Medicine, University of Missouri, 1600 E. Rollins Rd, Columbia, MO 65211, mohanr@health.missouri.edu.

[+]Present address: Department of Ophthalmology and Visual Sciences, Medical College of Wisconsin, Milwaukee, Wisconsin, USA.

None of the authors have any conflict of interest to disclose.

early tested times. Histological examinations revealed noticeably abnormal morphology and compromised collagen levels in injured *dcn*$^{-/-}$ corneas compared to the injured/normal *dcn*$^{+/+}$ and uninjured *dcn*$^{-/-}$ corneas. TEM analysis exhibited remarkably uneven collagen fibrils size and distribution in the stroma with asymmetrical organization and loose packing in injured *dcn*$^{-/-}$ corneas than injured/normal *dcn*$^{+/+}$ and uninjured *dcn*$^{-/-}$ corneas. The minimum and maximum inter-fibril distances were markedly irregular in injured *dcn*$^{-/-}$ corneas compared to all other corneas. Together, results of clinical, histological, and ultrastructural investigations in a genetic knockout model suggested that decorin influenced stromal fibrillogenesis and transparency in healing cornea.

Keywords

Cornea; Collagen fibrillogenesis; Decorin null mice (*dcn*$^{-/-}$); Transmission electron microscopy (TEM); Wound healing

1. Introduction

The cornea is a transparent and avascular tissue that provides two-thirds of the refractive power required for normal vision. Collagens are major structural component of the cornea within the tissue. The transparency and strength of the cornea arise from the highly organized spatial arrangement of the collagen fibrils and its interactions with stromal extracellular matrix organization (ECM) (Chen et al., 2015; Chaurasia et al., 2015). The mechanical strength and shape of the cornea are compactly related to the highly organized three-dimensional (3D) architecture of the corneal stroma (Gardner et al., 2015). In the stromal ECM, collagen fibrils are arranged in a high degree of lateral order with relatively uniform diameters throughout the stroma providing tensile strength and transparency to the corneal tissue (White et al., 2017). Corneal cells interact with a rich variety of *in vivo* biophysical stimuli: the stroma and basement membranes present them with a range of stiffnesses and complex topographies (Abrams et al., 2000).

Any trauma, like mechanical, surgical, chemical insults, etc. disturbs stromal fibril organization and affects corneal transparency, which eventually leads to fibrosis/scar formation and corneal neovascularization (CNV) (Gronkiewicz et al., 2016; Wilson et al., 2017). A plethora of research and clinical data reveals that in addition to cytokines and growth factors such as vascular endothelial growth factor (VEGF) (Mohan et al., 2011c), transforming growth factor-β (TGFβ) (Massague, 1998), a variety of other peptides and insoluble ECM macromolecules especially the reorganization of collagen fibrils are of utmost importance for the maintenance of corneal transparency (BenEzra et al., 1997). Corneal wounds result in the degradation, disorganization of collagen fibers, and rupture of collagen struts in the ECM of corneal tissue with compromised corneal transparency. The process of collagen fibrillogenesis regulates collagen synthesis and metabolism that regulates collagen fiber assembly and structural integrity changes (Weis et al., 2005). In collagen fibrillogenesis, the ECM has a prominent influence on cell behavior, influencing shape, polarity, movement, metabolism, modulating cell growth, differentiation,

and development (Brown et al., 2002). But how proteoglycans interact with the collagen architecture in the ECM during corneal wound healing has remained poorly understood.

Decorin is a small leucine-rich proteoglycan (SLRP) and accounts for nearly 40% of the total proteoglycans in the cornea (Gregory et al., 1982; Iozzo, 1998). It is shown to play an important role to regulate cellular structure, tissue organization, fibrillogenesis, tissue repair, and organization of ECM architecture (Lim et al., 2018; Mohan et al., 2010; Mohan et al., 2011a). The protein cores of these proteoglycans contain leucine-rich repeats in the central part of the molecule that forms a curved solenoid structure with convex and concave faces flanked by cysteine-rich domains on two sides. The individual proteoglycan core proteins are thought to bind with collagen fibrils at specific axial sites along the collagen fibrils (Meek and Knupp, 2015). Previous reports suggest that decorin plays an essential role in collagen fibrillogenesis and interacts with all major type I and II collagen-rich tissues and co-localizes with large helical collagen fibers (Mohan et al., 2011a). Therefore, collagen organization in the ECM assembly and its interactions with decorin are the critical events during corneal wound healing. The dcn null transgenic mouse ($dcn^{-/-}$) can provide an evidence and better understanding of the role of dcn in collagen tissue assembly and in collagen fibrillogenesis in corneal tissue. The $dcn^{-/-}$ mice are healthy, viable, and show no visible anatomical abnormalities (Reed and Iozzo, 2002). The body anatomy and weight of $dcn^{-/-}$ mice are of normal size like their wild type ($dcn^{+/+}$) strain. However, in $dcn^{-/-}$ mice, the collagen network in the skin was found loosely packed with irregular contours and lateral fusion of collagen fibrils (Brown et al., 2002; Danielson et al., 1997). While the eye appears normal and cornea maintains its integrity in $dcn^{-/-}$ mice, what happens to the cornea after trauma or injury is still unknown. In the present study, we sought to determine the functional role of dcn in the regulation of spatial arrangement of collagen fibrils at the ultrastructure levels with transmission electron microscopy in relevance to injury. Additionally, we graded corneal transparency clinically with Slit lamp microscope to recognize its impact during wound healing post-injury.

2. Materials and Methods

2.1. Animals

A heterozygous strain ($dcn^{+/-}$) breeding pair of C57BL/6J background was obtained from Renato V. Iozzo, PhD, Department of Pathology, Anatomy, and Cell Biology, and Translational Cellular Oncology Program, Thomas Jefferson University, Philadelphia, Pennsylvania, USA. The homozygous $dcn^{-/-}$ and wild-type ($dcn^{+/+}$) colonies were generated with by using multiple heterozygous strain ($dcn^{+/-}$) breeding pairs. In this study, decorin homozygous null ($dcn^{-/-}$) and wild type ($dcn^{+/+)}$ mice were used. The study was approved by the Institutional Animal Care and Use Committees of the Harry S. Truman Memorial Veterans' Hospital, Columbia, MO and the University of Missouri, Columbia, MO. Animals were treated in accordance with the ARVO Statement of the Use of Animals in Ophthalmic and Vision Research and housed in the animal facility under 12:12 hour light-dark cycle with ambient room temperature (25 °C) and *ad libitum* access to food and water. Anesthesia was performed in mice by intraperitoneal injection of a cocktail containing ketamine hydrochloride (100 mg/kg) and xylazine hydrochloride (10 mg/kg).

Topical ophthalmic anesthesia solution, proparacaine hydrochloride, was applied prior to any procedure. The study has four groups (*dcn*$^{-/-}$ with no corneal injury, *dcn*$^{-/-}$ with corneal injury, *dcn*$^{+/+}$ with no corneal injury and *dcn*$^{+/+}$ with corneal injury) and each group has 12 mice (6 males and 6 females) ranging 10–14 weeks of age. Eyes of each group are collected at day 3, 7, 14, and 21 post injury.

2.2. Induction of corneal injury

The corneal wound was generated in mouse eye by a well-established corneal alkali wounding procedure (Balne et al., 2021). Only one eye of each animal, selected randomly, was used for alkali wounding. In an anesthetized mouse, one drop of 0.5% proparacaine hydrochloride solution was instilled into the eye and then alkali injury was performed. In brief, alkali injury was produced by topically applying 2 mm diameter filter paper disc soaked in 0.5M sodium hydroxide (NaOH) for 30 seconds. The eye was then copiously washed with balanced salt solution (BSS) to remove NaOH. Thermal support was provided to animal throughout the procedure and during the recovery period.

2.3. Slit lamp biomicroscopic Imaging and clinical analysis

All mice underwent eye examination and imaging at regular intervals (day 3, 7, 14, and 21) after injury with a stereomicroscope equipped with a digital camera (SpotCam RT KE, Diagnostic Instruments Inc., USA). Eye health was evaluated using a slit lamp microscope (SL-15 portable Slit lamp, Kowa Optimed Inc. Torrance, CA, USA) as reported earlier (Fantes et al., 1990; Gupta et al., 2018; Mohan et al., 2011c).

2.4. Tissue Collection and Histology

Mice were humanely euthanized with an intraperitoneal injection of 150 mg/kg pentobarbital under ketamine/xylazine anesthesia. Eyeballs were collected for histology and corneas excised from globes for ultrastructural investigation. For histology, eyeballs enucleated from animals were placed immediately in optical cutting temperature (OCT) compound, snap-frozen, and stored at −80°C. For ultrastructural analysis, corneas were dissected from globes and immersed in TEM buffer following recently reported method (Sinha et al., 2021). Frozen tissues were sectioned at 8-μm thickness with a cryostat, placed on a glass slide, and stored frozen at −80°C until staining was performed following previously reported method (Gupta et al., 2017).

2.5. Transmission electron microscopy (TEM) Microscopy

The mouse corneal tissues were collected from experimental groups and immediately processed for TEM sample preparation. Unless otherwise stated, all reagents were purchased from Electron Microscopy Sciences, and all specimen preparation was performed at the Electron Microscopy Core Facility, University of Missouri, Columbia, MO. In brief, the dissected cornea tissue was washed with ice-cold 1X PBS divided into 3 pieces and immediately fixed in 2% paraformaldehyde + 2% glutaraldehyde containing 100 mM sodium cacodylate buffer (pH=7.35). Next, fixed tissues were rinsed with 100 mM sodium cacodylate buffer, (pH 7.35) containing 130 mM sucrose. Secondary fixation was performed using 1% osmium tetroxide (Ted Pella, Inc. Redding, California) in cacodylate buffer using

a Pelco Biowave (Ted Pella, Inc. Redding, California) operated at 100 Watts for 1 minute. Specimens were next incubated at 4°C for 1 hour, then rinsed with cacodylate buffer and further with distilled water. Using the Pelco Biowave, a graded dehydration series (per exchange, 100 Watts for 40sec) was performed using ethanol, transitioned into acetone, and dehydrated tissues were then infiltrated with epoxy resin (250 Watt for 3 min) and polymerized at 60°C overnight. For light microscopy, 0.5-μm sections were cut with an ultra-microtome (UC6; Leica EM, Wetzler, Germany), and the sections were stained with 1% toluidine blue.

For TEM, sections were cut to a thickness of 85 nm using an ultramicrotome (Ultracut UCT, Leica Microsystems, Germany) and a diamond knife (Diatome, Hatfield PA). These sections floated on distilled water and mounted on copper grids. The grids were dried and observed at magnifications 600–50000 X at 80 kV. Post-sectioning staining with uranyl acetate and Sato's lead stain was performed. A Transmission electron microscope (JEM-1400; JEOL, Peabody, MA) at 80 kV on a Gatan Ultrascan 1000 CCD (Gatan, Inc, Pleasanton, CA) equipped with a CCD camera (USC1000 2Kx2K; Gatan, Pleasanton, CA) and located at the Electron Microscopy Core Facility (University of Missouri) was used to collect images of each corneal layer from individual eyes of *dcn*$^{+/+}$ and *dcn*$^{-/-}$ mice.

2.6. Biocomputing and TEM image data analysis

Collagen fibril arrangement was analyzed in cross-section of TEM images taken from mid stromal region between the anterior and posterior stromal areas (Figure 3E) by computing 10 fibers per image in six to nine images for each experimental group. The fibril area, diameters, and inter fibril distances in all TEM images were quantified using automatic image analysis software developed and reported previously (Gronkiewicz et al., 2016). In brief, it consists of four main modules: (i) image preprocessing, (ii) fibril segmentation, (iii) fibril shape analysis and cluster decomposition, and (iv) size and inter-fibrillar distance analysis. The details given below.

2.6.1. Image Preprocessing—The image processing step involved noise removal using linear and non-linear image filtering, specifically using Gaussian and median filters and normalization of uneven background from the original TEM images. The image background (regions not occupied by collagen fibrils) was modeled by polygonal surface fitting to the local gray-level intensity maxima. Matlab software (Matlab 2019) curve or surface fitting function with quadratic polygon fitting option was used to model the image background. This processing is important for removing background intensity bias while automatically locating the fibril cross-sections in the TEM images.

2.6.2. Fibril Segmentation—TEM image segmentation refers to the process of partitioning or dividing an image into non-overlapping regions with similar attributes (i.e. intensity, color, texture, shape etc.) that are meaningful for the particular application in hand. This step aims to partition the input images into regions occupied by collagen fibril cross-sections versus by background. Fibril segmentation process was performed using a combination of intensity-based threshold and Hessian-based blob detection approaches. The obtained segmentation mask was post-processed with mathematical morphology operations

to remove small spurious detections and to fill small holes. Hessian matrix (Equation 1) describes the second-order structure of local intensity variations around each point of the image L (x, y). Eigenvalues $\lambda_{1,2}$ (Equation 2) of the Hessian matrix can be used to detect blob-like, or ridge-like structures (Frangi et al., 1998). Table 2 shows possible local orientation patterns based on the eigenvalues of the Hessian matrix.

$$\mathbf{Hessian}_{\sigma}(x, y) = \begin{bmatrix} L_{xx}(x, y) & L_{xy}(x, y) \\ L_{xy}(x, y) & L_{yy}(x, y) \end{bmatrix} \tag{1}$$

$$\lambda_{1,2} = \frac{1}{2}\left(L_{xx} + L_{yy} \pm \sqrt{\left(L_{xx} - L_{yy}\right)^2 + \left(2L_{xy}\right)^2}\right) \tag{2}$$

Hessian matrix was computed by convolving the TEM image with derivatives of the Gaussian kernel where scale σ represents the standard deviation of the Gaussian kernel and controls the radius of the detected structures. Initial coarse segmentation of the fibril cross-sections was generated by computing Hessian matrix and threshold λ_1(Hessian) was calculated (Equation 3)

$$Mask_{Fibril}(x, y) = \begin{cases} 1 & \lambda_1(\mathbf{Hessian}(x, y)) < \varepsilon \\ 0 & \text{otherwise} \end{cases} \tag{3}$$

2.6.3. Shape Analysis and Cluster Decomposition—The shape analysis and cluster decomposition module were applied to refine the initial segmentation masks to identify individual collagen fibrils accurately after efficient detection of segment regions occupied by fibrils free from the factors such as noise, background structures, low contrast, weak or blurred boundaries, and intensity variations following our reported earlier methods (Ersoy et al., 2012; Sun et al., 2014; Gronkiewicz et al., 2016;). To refine segmentation, first connected component labeling was applied to the mask and disconnected blobs B_i were determined, and their areas were computed. Ellipses (E_i) were then fitted to each blob (B_i) and ellipse areas were calculated. Larger blobs with area difference ratio (ADR) were larger than a threshold, an indication of large deviation from the elliptical shape were further processed by cluster decomposition module to segment individual fibrils within the cluster (Equation 4).

$$ADR = \frac{area(Ei) - area(Bi)}{area(Bi)} \tag{4}$$

Marker-controlled watershed transformation (Vincent, 1991) was used to decompose fibril clusters into individual fibrils. Regional maxima of distance transform were used as markers. To suppress spurious regional maxima and to prevent over-segmentation H-maxima transform (Soille, 2003) was applied to the distance transform prior to the detection of regional maxima. The obtained masks were visually inspected and in very rare cases were manually corrected to ensure correct quantitative analysis.

2.6.4. Fibril Size and Inter-fibrillar Distance (IFD) Analysis—This module computes parameters related to fibril morphology and spacing such as fibril radius and inter-fibrillar distance. From the refined segmentation mask obtained after cluster decomposition, fibril cross-section areas and centroids were computed. Since blob major axis length is more affected by sample preparation (e.g., diagonal cross-sections result in larger major axis), blob minor axis length was used as an estimate of the fibril radius. Delaunay triangulation & vertex coloring were applied to fibril centroids to construct a colored neighborhood graph (Nath et al., 2006; Ersoy et al., 2012; Gronkiewicz et al., 2016). In the neighborhood graph, nodes correspond to individual fibrils and the edges link to immediate neighbors. For each node in this neighborhood graph, two specific neighbors, a nearest immediate neighbor, and a farthest immediate neighbor were identified. A second graph, the nearest/farthest neighborhood graph, was constructed using only these specific links. On these created neighborhood graphs, distance from a fibril to its nearest immediate neighbor fibril was termed as minimum inter fibril distance (min IFD) and distance from a fibril to its farthest immediate neighbor fibril was termed as maximum inter fibril distance (max IFD). Fibril-to-fibril interactions and spatial organization of collagen fibrils were quantified using these two neighborhood graphs (Nath et al., 2006; Ersoy et al., 2012; Gronkiewicz et al., 2016, Sinha et al. 2021).

2.7. Morphometric and Histopathological analysis of Masson's Trichrome and periodic acid-Schiff (PAS) stained corneal sections

Masson's Trichrome and PAS staining are used to characterize the severity of the collagen organization, collagen production, and glycoprotein pattern in the anterior to posterior corneal tissue. Serial transverse corneal sections obtained after routine histologic processing (8 μm sections) were mounted on glass slides for staining with Masson's Trichrome and periodic acid-Schiff (PAS) for comparative morphometric evaluation as described previously (Gronkiewicz et al., 2016; Gupta et al., 2018). After each staining, the morphometric evaluations of slides were performed using light microscopy. Corneal tissue sections were analyzed for any histopathological abnormalities.

2.8. Statistical Analysis

Statistical analysis was performed with GraphPad Prism 8 software (GraphPad Software, Inc., San Diego, CA, USA). The results were expressed as the mean ± standard error of the mean (SEM). A priori power statistical G*Power 3.0.10 software was used for power, effect, and sample size calculations (Faul et al., 2007). Statistical analysis was performed with Student's t-test and one-way analysis of variance (ANOVA) followed by post hoc test in different experimental groups. A value of $p<0.05$ was considered statistically significant.

3. Results

3.1. Clinical observation and grading of haze and CNV

To test the role of *dcn* gene in collagen fibrillogenesis during corneal wound healing, an alkali induced *in vivo* mice model ($dcn^{+/+}$ and $dcn^{-/-}$) was used. A time-dependent comparative responses of injury on $dcn^{+/+}$ and $dcn^{-/-}$ corneas were shown in slit-lamp microscopic images (Figure 1). The slit-lamp microscopic images showed a vital role of

decorin in corneal transparency and wound healing response in both *dcn*$^{+/+}$ (Figure 1B–E) and *dcn*$^{-/-}$ (Figure 1G–J) groups as compared to the corresponding no-injury groups (Figure 1A & F). At day 21, the *dcn*$^{-/-}$ strain showed the more prominent haze and less transparent area in corneal tissue (Figure 1J) when compared to the *dcn*$^{+/+}$ strain (Figure 1E). At day 3, 7, and 14, no appreciable differences in corneal haze or neovascularization score were observed in *dcn*$^{-/-}$ (Figure 1G–I) versus *dcn*$^{+/+}$ (Figure 1B–D) animals. Also, eyes of the no-injury control groups of both the *dcn*$^{+/+}$ and *dcn*$^{-/-}$ demonstrated the avascular, clear, and normal corneas (Figure 1A & F).

The corneal haze was quantified in a masked manner using Fantes haze grading scale and slit-lamp microscope. At day 21, a significantly higher haze was observed in *dcn*$^{-/-}$ after alkali injury ($p < 0.001$; Figure 2A) compared to the *dcn*$^{+/+}$. Likewise, *dcn*$^{-/-}$ mice showed a significantly higher corneal neovascularization compared to *dcn*$^{+/+}$ after alkali injury at day 21 ($p < 0.001$; Figure 2B) but and at earlier times. The corneal haze and neovascularization levels in injured *dcn*$^{+/+}$ and *dcn*$^{-/-}$ animals at the day 3, 7, or 14 were clinically relevant but found statistically insignificant. All uninjured corneas of the *dcn*$^{+/+}$ and *dcn*$^{-/-}$ were transparent and avascular cornea.

3.2. Ultrastructure changes and role of decorin protein in collagen fibrillogenesis

The collagen fibrillogenesis and role of decorin were analyzed using the TEM high magnification images, and the structural changes were quantified using the Biocomputing software tools (Figure 3). The reference images represent the analysis pattern and quantification procedure used in the study for all different groups. Figure 3A shows the original TEM images at 25,000 X magnification; Figure 3B shows the segmentation pattern where green color ellipses are fitted to individual blobs, black lines denote ellipse minor axes and red dot denotes the blob centroid. In the same way, Figure 3C portrays fibril centroids and fibril neighborhood graphs while Figure 3D red and blue connecting lines symbolize minimum IFD and maximum IFD, respectively.

3.3. Collagen fibril distribution and lateral packing

The distribution and arrangement of fibrils at ultrastructural level in corneas were analyzed using TEM images taken at 1500x from ultrathin sections of the uninjured and injured corneas of the *dcn*$^{+/+}$ and *dcn*$^{-/-}$ mice at day 21 (Figure 4). The zone of analysis for the ultrastructural investigation is shown in Figure 4E. The corneas of injury groups of *dcn*$^{+/+}$ and *dcn*$^{-/-}$ mice revealed highly disrupted fibril distribution, organization, and packing (Figure 4C & D) compared to the corneas of the corresponding no-injury groups (Figure 4A & B). The injured *dcn*$^{-/-}$ corneas showed numerous non-parallel and loose packing of collagen fibrils (Figure 4D and magnified inset) compared to the injured *dcn*$^{+/+}$ (Figure 4C and magnified inset). The TEM images of no-injury groups of *dcn*$^{+/+}$ (Figure 4A and magnified inset) and *dcn*$^{-/-}$ (Figure 4B and magnified inset) corneas showed typical dense packing and organized collagen fibril distribution.

3.4. Collagen fibril area and diameter arrangement showing the frequency of distribution in dcn$^{+/+}$ and dcn$^{-/-}$ mice

To quantify changes in distribution pattern and packing of collagen fibrils in the uninjured and injured corneas of the *dcn*$^{+/+}$ and *dcn*$^{-/-}$ mice, fibril area, diameter, and inter fibril distances (IFD) were measured using TEM images collected at 25,000X magnification. The corneas of the *dcn*$^{+/+}$ and *dcn*$^{-/-}$ mice revealed substantial changes in collagen fibril area, diameter, and minimum/maximum IFDs after injury (Figure 5C & D). Further, fibrils in injured *dcn*$^{-/-}$ corneas were poorly distributed and unevenly packed (Figure 5D) than the *dcn*$^{+/+}$ corneas (Figure 5C). It was evident from the ultrastructure images of corneas that the collagen fibrils did not have a perfect hexagonal lattice. The images depicted that the geometry of the adjacent collagen fibrils was not systematic in *dcn*$^{+/+}$ and *dcn*$^{-/-}$ mice (no-injury and alkali injury). The changes in adjacent collagen fibril distances were likely due to a consequence of the balancing of two opposite forces interim on fibrils brought by the decorin proteoglycans (Meek and Knupp, 2015). The TEM comparative analysis of *dcn*$^{+/+}$ and *dcn*$^{-/-}$ corneas indicated the importance of decorin protein in corneal stromal fibrillogenesis.

In corneal stroma, the collagen particles are organized in a regular fashion and create a unique crystal-like fibril arrangement. This unique distribution of collagen fibrils has the advantage for the quantification of collagen fibril distribution patterns. To study the collagen organization at the nanoscale in the corneal stroma, TEM analysis was performed to visualize and quantify structural changes about the collagen fibrils area and diameter using biocomputing tools. The comparisons of collagen fibril distribution and area of collagen fibril cross-sections are presented in Figure 6. We found that the collagen fibril area of the no-injury group was tightly clustered (Figure 6A & B) (*dcn*$^{+/+}$ mice: average area pixels: 3736, SEM: 29 and *dcn*$^{-/-}$ mice: average area pixels: 3604, SEM: 25). On the contrary, the distribution of collagen fibril area of injury group was loosely clustered (Figure 6C & D) (*dcn*$^{+/+}$ mice: average area pixels: 2917, SEM: 24 and *dcn*$^{-/-}$ mice: average area pixels: 4303, SEM: 30). The comparative area distribution graph of *dcn*$^{-/-}$ corneas after injury (Figure 6E) showed significant changes in area pixel as compared to *dcn*$^{+/+}$ mice after injury (area pixels 4303 and 2917 respectively; $p<0.001$) revealing the role of decorin protein in collagen fibril organization.

The diameter of each collagen fibril was also measured using the masking of each collagen fibril (Figure 7) in corneas of *dcn*$^{+/+}$ and *dcn*$^{-/-}$ mice (no-injury and injury). The wide distribution of collagen fibril diameter in *dcn*$^{-/-}$ mice suggested impaired lateral packing. The histogram graph represented the frequency of collagen fibril diameter of *dcn*$^{-/-}$ corneas randomly in size of 65–70 pixels; (Figure 7B & D) while the frequency of collagen fibril diameter of *dcn*$^{+/+}$ corneas in size of 45–65 pixels (Figure 7A & C). The structural changes in the corneas of the *dcn*$^{-/-}$ mice after injury were depicted by the non-uniform collagen fibril diameter and abnormal packing. The corneal TEM images and the biocomputing pattern of collagen fibril diameter demonstrated a significant reduction in collagen fibril diameter between the two different genotypes after injury, and this was consistent in the radial zone of injury. The collagen fibril diameter remained constant, and no noticeable changes were recorded in *dcn*$^{+/+}$ and *dcn*$^{-/-}$ non-injured corneas (Figure 7E). The altered

distribution of collagen fibril orientation, area, and diameter from injury to a no-injury condition in the stroma indicated a transition of anisotropic microstructure in *dcn*$^{+/+}$ mice to a more orthotropic microstructure in *dcn*$^{-/-}$ mice. Together, these data demonstrated that injured *dcn*$^{-/-}$ corneas had poorly organized collagen fibrils compared to *dcn*$^{+/+}$ corneas and supported the hypothesis that decorin protein plays a role in collagen fibril assembly.

3.5. Inter fibril distance depicting the collagen fibril distribution pattern in dcn$^{+/+}$ and dcn$^{-/-}$ mice

Inter fibril distance (IFD) pattern defines the smoothness of collagen fibrillogenesis and spatial organization in the cornea. The min and max IFD analysis of each collagen fibril showed the organization and distribution pattern of fibrillogenesis in four experimental groups (Figure 8). The red-connecting lines represent min IFD, while blue-connecting lines represent max IFD of each collagen fibril. The TEM masking figure demonstrated the min and max IFD pattern in each group as evident from loose and tight organization of collagen fibrils (Figure 8). We found alteration in measurements of average collagen inter-fibril spacing and corresponding images revealing higher and random fibril spacing in the injury groups (Figure 8C & D) of *dcn*$^{+/+}$ and *dcn*$^{-/-}$ mice compared to the no-injury groups (Figure 8A & B), respectively.

Similarly, the min IFD and max IFD of collagen fibrils were measured using the masking of each collagen fibril in *dcn*$^{+/+}$ and *dcn*$^{-/-}$ corneas (no-injury and injury groups) using a biocomputing tool (Figure 9). The min and max IFDs of entire fibril population of *dcn*$^{+/+}$ and *dcn*$^{-/-}$ corneas of no-injury and injury groups were analyzed and plotted as violin graphs (Figure 9). The comparisons of IFD data showed uniform arrangement (Figure 9A & B) in non-injured corneas of the *dcn*$^{+/+}$ and *dcn*$^{-/-}$ mice. Biocomputing and statistical analysis of the min/max IFD of non-injured *dcn*$^{+/+}$ and *dcn*$^{-/-}$ (average minimum IFD 107±0.5 and 118±0.7, and average maximum IFD 284±6.6 and 286±6.1) showed no significant changes ($p>0.05$). On the other hand, the comparative analysis of IFD graphs of injured-corneas of the *dcn*$^{+/+}$ and *dcn*$^{-/-}$ mice showed the random and jagged distribution of collagen fibrils (Figure 9C & D). The violin graph shows min IFD and max IFD in injured corneas of *dcn*$^{+/+}$ and *dcn*$^{-/-}$ mice (average minimum IFD 81±0.3 and 108±0.8, and average maximum IFD 200±4.9 and 310±7.5) that were found statistically significant ($p<0.05$). The mean of min and max IFDs (Figure 9E & F) of collagen fibrils in *dcn*$^{+/+}$ and *dcn*$^{-/-}$ showed significant changes in the injured groups when compared with the no-injury groups. Overall, this analysis reflects that injury in *dcn*$^{-/-}$ cornea caused disorganization of collagen fibril distribution pattern.

3.6. Histology evaluation, collagen level changes and role of proteoglycan in collagen fibrillogenesis in dcn$^{+/+}$ and dcn$^{-/-}$ mice

The changes in corneal morphology and collagen were studied with PAS (Figure 10) and Masson's trichrome staining (Figure 11). The PAS staining showed remarkable morphologic alterations in injured corneas of *dcn*$^{-/-}$ and *dcn*$^{+/+}$ mice (Figure 10C & D) but not in non-injured eyes (Figure 10A & B) at day 21. Similarly, the Masson's trichrome staining showed noticeable changes in collagen levels in injured corneas (Figure 10C & D) compared to the non-injured corneas of *dcn*$^{+/+}$ and *dcn*$^{-/-}$ mice (Figure 11A & B). An expected neo

blood vessels were observed in alkali injured corneas of the *dcn*$^{-/-}$ and *dcn*$^{+/+}$ (Figure 11C & D) but not in non-injured eyes (Figure 11A & B) mice at day 21. A montage of PAS stained images taken at 40x magnification from injured *dcn*$^{-/-}$ and *dcn*$^{+/+}$ corneal sections revealed greater neovascularization in the injured *dcn*$^{-/-}$ corneas (Figure 11F) compared to the *dcn*$^{+/+}$ corneas (Figure 11E), No neovascularization was observed in uninjured *dcn*$^{-/-}$ and *dcn*$^{+/+}$ corneas (data not shown).

4. Discussion

The corneal stroma consists of three primary non-aqueous constituents: collagens, proteoglycans, and cells (Meek and Knupp, 2015). The cornea is unique among connective tissues in exhibiting high mechanical strength and transparency. This is made possible with the highly specialized organization of collagen fibrils embedded in a hydrated fibrillar matrix (Boote et al., 2011) of the corneal stroma. The well-organized and uniform pattern of fibrils with multiple lamellae in ECM provides transparency and strength to the corneal tissue (Boote et al., 2011; Komai and Ushiki, 1991; Maurice, 1957). The shape of the corneal tissue is prospectively influenced by the size and arrangement of collagen fibrils between tissue regions (Meek and Knupp, 2015).

Collagens play a key role in maintaining corneal shape, size, and refractive properties through their distinctive uniform diameter and arrangement with a high degree of definite ordering (Sinha et al. 2021). The major collagens in the cornea are type I, III, V, VI, and XIII. The arrangement, disarrangement, and rearrangement of collagen fibrils in extracellular matrices are dynamic processes and affect corneal function. Previous studies show that the collagen fibrils in corneal stroma are embedded with proteoglycans (Hoffman et al., 1957; Meyer and Anderson, 1965). The distribution of collagen lamellae, organization, and IFD are important for normal corneal function and wound healing. The normal human corneal stroma contains four small leucine-rich proteoglycans: decorin, lumican, keratocan, and mimecan. The c-terminal capping motifs in decorin, lumican, and keratocan have an “ear repeat”, a leucine-rich repeat that extends outward from the convex face and probably helps to maintain protein conformation and collagen-binding ability (Meek and Knupp, 2015; Meek and Leonard, 1993). The individual proteoglycan core proteins are thought to bind to collagen fibrils at specific axial sites along the collagen fibrils (Meek and Holmes, 1983; Scott and Haigh, 1988). The fibril organization in corneal stroma is tissue-specific and perhaps affected by the molar ratios and spatial distributions of fibrils, non-collagenous macromolecules associated with the fibril, and assembly conditions. The present study mainly focuses on analyzing the compositional aspects of fibril assembly in the stroma of an uninjured and injured corneas of the *dcn*$^{-/-}$ and *dcn*$^{+/+}$ mice at ultrastructural level to better understand its role in corneal function.

The precise organization of collagen fibrils in stroma is paramount to corneal refractive and transparent properties (Hassell and Birk, 2010). With the advent of new computational tools to quantify TEM imaging data, it has become possible to collect precise information about the distinctive collagen fibril organization in stroma and its relevance in the context of corneal transparency. The current work expands on this by examining alterations in collagen fibrillogenesis in −/+ injury and −/+ decorin *in vivo*. In the cornea, decorin is

synthesized by the stromal fibroblasts/keratocytes in the ECM network and has an ability to interact with various growth factor and receptors such as transforming growth factor beta, epithelial growth factor receptor, pigmented epithelium derived factor, vascular endothelial growth factor, etc. and regulate their biological activities (Mohan et al., 2010, 2011b, 2019). The glycosaminoglycans (GAGs) side chain of the decorin can intermingle with stromal fibrils and act as a reservoir of growth factors. Decorin can fill the interstitial spaces within a tissue microenvironment and facilitate ECM interactions by acting as a ligand for cell surface receptors (Baghy et al., 2012; Fust et al., 2005). The chopping of the ECM with GAGs regulates the ECM architecture. However, interactions of decorin with growth factors, cytokines, and ECM molecules are complex and tightly regulated in tissue homeostasis and wound repair in ocular and non-ocular tissues (Bonnans et al., 2014; Mohan et al., 2011b; Kamil and Mohan 2021). Our previous reports exhibited the role of decorin in modulating corneal wound healing, fibrosis, and neovascularization using gain-of-function model by delivering decorin gene into human corneal fibroblasts *in vitro* (Mohan et al., 2010) and rabbit cornea *in vivo* (Mohan et al., 2011a; 2011c). The current study shows the role of decorin in modulating corneal collagen fibrillogenesis using a loss-of-function *in vivo* mouse model. To the best of our knowledge, this is the first study with decorin null mice to exhibit that ocular injury disrupts characteristic spatial arrangement of fibrils in stroma and corneal integrity *in vivo*.

There are many limitations to our present study. Proteoglycans play an important role in extending mechanical properties to the cornea and other ocular and non-ocular tissues (Fust et al., 2004; Quantock and Young 2008; Hatami-Marbini and Pinsky, 2010). In the present study, we did not investigate the effects of decorin on mechanical properties of the cornea and how they impact normal corneal function. The cornea is known to express other SLPRs such as biglycan and lumican besides decorin (Mohan et al. 2010b). Both, decorin and biglycan share a common binding site for collagen I but decorin binds to collagen I with greater affinity than the biglycan (Robinson et al., 2017). In this study, we did not examine the effects of biglycan, if any, on stromal fibrillogenesis following injury. Furthermore, utilized decorin null mice are truncated decorin knockouts, thereby the observed changes in the stromal fibrillogenesis within the cornea and vision loss after injury may be more than reported in this study. In present study, we observed significantly less haze and neovascularization (Figure 1, 2, 10, &11) and disruption in the distinctive stromal fibrillogenesis (Figure 4–9) in injured $dcn^{-/-}$ mouse corneas at day 21 compared to the $dcn^{+/+}$ corneas under similar injury condition. It led us to speculate that the rescue effects of decorin on corneal wound healing events post injury are time depended. However, we did not use multiple late timepoints in the study, and therefore unable to tell if observed rescue of corneal irregularities by decorin remain same, get worst, or improve over time.

In conclusion, present study demonstrates the effects of decorin in regulating collagen fibrillogenesis in stroma of the normal and healing cornea *in vivo* using decorin null and wild type mice in conjunction with a standard injury technique.

Acknowledgments

This work was primarily supported by the NEI/NIH R01EY017294, R01EY030774, and U01EY031650 grants (RRM), and partial support from the United States Department of Veterans Health Affairs Merit 1I01BX00357 and IK6BX005646 Senior Research Career Scientist grants (RRM), and Ruth M. Kraeuchi Missouri Endowed Chair Ophthalmology University of Missouri Fund (RRM). The authors thank Ashika Srivastava, an intern, for her help in assembling the manuscript draft.

References

Abrams GA, Schaus SS, Goodman SL, Nealey PF, Murphy CJ, 2000. Nanoscale topography of the corneal epithelial basement membrane and Descemet's membrane of the human. Cornea. 19, 57–64. 10.1097/00003226-200001000-00012. [PubMed: 10632010]

Baghy K, Iozzo RV, Kovalszky I, 2012. Decorin-TGFβ axis in hepatic fibrosis and cirrhosis. J Histochem Cytochem. 60(4), 262–268. https://doi:10.1369/0022155412438104. [PubMed: 22260996]

Balne PK, Gupta S, Zhang J, Bristow D, Faubion M, Heil SD, Sinha PR, Green SL, Iozzo RV, Mohan RR, 2021. The functional role of decorin in corneal neovascularization in vivo. Exp. Eye Res 207, 108610. 10.1016/j.exer.2021.108610. [PubMed: 33940009]

BenEzra D, Griffin BW, Maftzir G, Sharif NA, Clark AF, 1997. Topical formulations of novel angiostatic steroids inhibit rabbit corneal neovascularization. Invest. Ophthalmol. Vis. Sci 38(10), 1954–62. [PubMed: 9331259]

Bonnans C, Chou J, Werb Z, 2014. Remodelling the extracellular matrix in development and disease. Nat Rev Mol Cell Biol. 15(12), 786–801. 10.1038/nrm3904. [PubMed: 25415508]

Boote C, Kamma-Lorger Christina S., Hayes S, Harris J, Burghammer M, Hiller J, Terrill, Nicholas J, Meek Keith M., 2011. Quantification of Collagen Organization in the Peripheral Human Cornea at Micron-Scale Resolution. Biophys. J 101(1), 33–42. 10.1016/j.bpj.2011.05.029. [PubMed: 21723812]

Brown CT, Lin P, Walsh MT, Gantz D, Nugent MA, Trinkaus-Randall V, 2002. Extraction and purification of decorin from corneal stroma retain structure and biological activity. Protein Expr. Purif 25, 389–399. 10.1016/S1046-5928(02)00025-6 [PubMed: 12182818]

Chaurasia SS, Lim RR, Lakshminarayanan R, Mohan RR., 2015. Nanomedicine approaches for corneal diseases. J. Funct. Biomater 6, 277–298. 10.3390/jfb6020277. [PubMed: 25941990]

Chen S, Mienaltowski MJ, Birk DE, 2015. Regulation of corneal stroma extracellular matrix assembly. Exp. Eye Res 133, 69–80. 10.1016/j.exer.2014.08.001. [PubMed: 25819456]

Danielson KG, Baribault H, Holmes DF, Graham H, Kadler KE, Iozzo RV, 1997. Targeted disruption of decorin leads to abnormal collagen fibril morphology and skin fragility. J. Cell Biol 136, 729–743. 10.1083/jcb.136.3.729. [PubMed: 9024701]

Ersoy I, Bunyak F, Higgins JM, Palaniappan K, 2012. Coupled edge profile active contours for red blood cell flow analysis, 2012 9th IEEE International Symposium on Biomedical Imaging (ISBI), pp. 748–751. 10.1109/ISBI.2012.6235656.

Fantes FE, Hanna KD, Waring GO 3rd, Pouliquen Y, Thompson KP, Savoldelli M, 1990. Wound healing after excimer laser keratomileusis (photorefractive keratectomy) in monkeys. Arch. Ophthalmol 108, 665–675. 10.1001/archopht.1990.01070070051034. [PubMed: 2334323]

Faul F, Erdfelder E, Lang A-G, Buchner A, 2007. G*Power 3: A flexible statistical power analysis program for the social, behavioral, and biomedical sciences. Behav. Rea. Methods 39, 175–191. 10.3758/bf03193146.

Frangi AF, Niessen WJ, Vincken KL, Viergever MA, 1998. Multiscale vessel enhancement filtering, in: Wells WM, Colchester A, Delp S (Eds.), Med. Image Comput. Comput Assist. Interv Springer Berlin Heidelberg, Germany, pp. 130–137. 10.1007/BFb0056195.

Fust A, LeBellego F, Iozzo RV, Roughley PJ, Ludwig MS, 2005. Alterations in lung mechanics in decorin-deficient mice. Am. J. Physiol. Lung Cell. Mol. Physiol 288 (1), L159–66. 10.1152/ajplung.00089.2004. [PubMed: 15447936]

Gardner S, Gardner SJ, White N, Albon J, Knupp C, Kamma-Lorger CS, Meek KM, 2015. Measuring the refractive Index of bovine corneal stromal cells using quantitative phase imaging. Biophys. J 109(8), 1592–1599. 10.1016/j.bpj.2015.08.046. [PubMed: 26488650]

Gregory JD, Cöster L, Damle SP, 1982. Proteoglycans of rabbit corneal stroma. Isolation and partial characterization. J. Biol. Chem 257(12), 6965–6970. [PubMed: 7085613]

Gronkiewicz KM, Giuliano EA, Kuroki K, Bunyak F, Sharma A, Teixeira LBC, Hamm CW, Mohan RR, 2016. Development of a novel *in vivo* corneal fibrosis model in the dog. Exp. Eye Res 143, 75–88. 10.1016/j.exer.2015.09.010. [PubMed: 26450656]

Gupta S, Fink MK, Ghosh A, Tripathi R, Sinha PR, Sharma A, Hesemann NP, Chaurasia SS, Giuliano EA, Mohan RR, 2018. Novel combination BMP7 and HGF gene therapy instigates selective myofibroblast apoptosis and reduces corneal haze *in vivo*. Invest. Ophthalmol. Vis. Sci 59, 1045–1057. 10.1167/iovs.17-23308. [PubMed: 29490341]

Gupta S, Rodier JT, Sharma A, Giuliano EA, Sinha PR, Hesemann NP, Ghosh A, Mohan RR, 2017. Targeted AAV5-Smad7 gene therapy inhibits corneal scarring *in vivo*. PLoS One. 12(3):e0172928. 10.1371/journal.pone.0172928. [PubMed: 28339457]

Hassell JR, Birk DE, 2010. The molecular basis of corneal transparency. Exp. Eye Res 91(3), 326–35. 10.1016/j.exer.2010.06.021. [PubMed: 20599432]

Hatami-Marbini H, Pinsky PM, 2010. "The contribution of proteoglycans on the mechanical properties of the corneal stroma." Proceedings of the ASME 2010 First Global Congress on Nano-Engineering for Medicine and Biology; 299–300. 10.1115/NEMB2010-13175.

Hoffman P, Linker A, Meyer K, 1957. The acid mucopolysaccharides of connective tissues. II. Further experiments on chondroitin sulfate B. Arch. Biochem. Biophys 69, 435–440. 10.1016/0003-9861(57)90508-8. [PubMed: 13445215]

Iozzo RV, 1998. Matrix proteoglycans: from molecular design to cellular function. Annu. Rev. Biochem 67, 609–52. 10.1146/annurev.biochem.67.1.609. [PubMed: 9759499]

Kamil S, Mohan RR, 2021. Corneal stromal wound healing: Major regulators and therapeutic targets. Ocul. Surf 19, 290–306. 10.1016/j.jtos.2020.10.006. [PubMed: 33127599]

Komai Y, Ushiki T, 1991. The three-dimensional organization of collagen fibrils in the human cornea and sclera. Invest. Ophthalmol. Vis. Sci 32(8), 2244–58. [PubMed: 2071337]

Lim R, Gupta S, Grant D, Sinha PR, Mohan R, Chaurasia S, 2018. Retinal ultrastructural and microvascular defects in decorin deficient ($dcn^{-/-}$) mice. Microsc. Microanal 24(S1), 1264–65. https://doi.org/doi:10.1017/S1431927618006803.

Massague J, 1998. TGF-beta signal transduction. Annu. Rev. Biochem 67, 753–91. 10.1146/annurev.biochem.67.1.753. [PubMed: 9759503]

Matlab, 2019. Version 9.6.0 (R2019a), Natick, Massachusetts: The MathWorks Inc.

Maurice DM, 1957. The structure and transparency of the cornea. J. Physiol 136, 263–286. 10.1113/jphysiol.1957.sp005758. [PubMed: 13429485]

Meek KM, Holmes DF, 1983. Interpretation of the electron microscopical appearance of collagen fibrils from the corneal stroma. Int. J. Biol. Macromol 5(1), 17–25. 10.1016/0141-8130(83)90073-9.

Meek KM, Knupp C, 2015. Corneal structure and transparency. Prog Retin Eye Res 49, 1–16. 10.1016/j.preteyeres.2015.07.001. [PubMed: 26145225]

Meek KM, Leonard DW, 1993. Ultrastructure of the corneal stroma: a comparative study. Biophys. J 64, 273–280. 10.1016/S0006-3495(93)81364-X. [PubMed: 8431547]

Meyer K, Anderson B, 1965. The chemical specificity of the mucopolysaccharides of the cornea. Exp. Eye Res 4, 346–348. 10.1016/s00144835(65)80050-1. [PubMed: 4222437]

Mohan RR, Gupta R, Mehan MK, Cowden JW, Sinha S, 2010. Decorin transfection suppresses profibrogenic genes and myofibroblast formation in human corneal fibroblasts. Exp. Eye Res 91, 238–245. 10.1016/j.exer.2010.05.013. [PubMed: 20546727]

Mohan RR, Tandon A, Sharma A, Cowden JW, Tovey JCK, 2011a. Significant inhibition of corneal scarring in vivo with tissue-selective, targeted AAV5 decorin gene therapy. Invest. Ophthalmol. Vis. Sci 52(7), 4833–41. 10.1167/iovs.11-7357. [PubMed: 21551414]

Mohan RR, Tovey JC, Gupta R, Sharma A, Tandon A, 2011b. Decorin biology, expression, function, and therapy in the cornea. Curr. Mol. Med 11(2), 110–28. 10.2174/156652411794859241. [PubMed: 21342131]

Mohan RR, Tovey JC, Sharma A, Schultz GS, Cowden JW, Tandon A, 2011c. Targeted decorin gene therapy delivered with adeno-associated virus effectively retards corneal neovascularization in vivo. PLoS One 6(10), e26432. 10.1371/journal.pone.0026432. [PubMed: 22039486]

Mohan RR, Tripathi R, Sharma A, Sinha PR, Giuliano EA, Hesemann NP, Chaurasia SS, 2019. Decorin antagonizes corneal fibroblast migration via caveolae-mediated endocytosis of epidermal growth factor receptor. Exp. Eye Res 180, 200–207. https://doi.10.1016/j.exer.2019.01.001. [PubMed: 30611736]

Nath SK, Palaniappan K, Bunyak F, 2006. Cell segmentation using coupled level sets and graph-vertex coloring. Med. Image Comput. Comput Assist. Interv 9(1), 101–108. 10.1007/11866565_13.

Quantock AJ, Young RD, 2008. Development of the corneal stroma, and the collagen–proteoglycan associations that help define its structure and function. Dev Dyn. 237, 2607–2621. 10.1002/dvdy.21579. [PubMed: 18521942]

Reed CC, Iozzo RV, 2002. The role of decorin in collagen fibrillogenesis and skin homeostasis. Glycoconj. J 19(4), 249–55. 10.1023/A:1025383913444. [PubMed: 12975602]

Robinson KA, Sun M, Barnum CE, Weiss SN, Huegel J, Shetye SS, Lin L, Saez D, Adams SM, Iozzo RV, Soslowsky LJ, Birk DE, 2017. Decorin and biglycan are necessary for maintaining collagen fibril structure, fiber realignment, and mechanical properties of mature tendons. Matrix Biol. 64, 81–93. https://doi: 10.1016/j.matbio.2017.08.004. [PubMed: 28882761]

Scott JE, Haigh M, 1988. Identification of specific binding sites for keratan sulphate proteoglycans and chondroitin-dermatan sulphate proteoglycans on collagen fibrils in cornea by the use of cupromeronic blue in 'critical-electrolyte-concentration' techniques. Biochem. J 253(2), 607–10. 10.1042/bj2530607. [PubMed: 2972275]

Sinha NR, Balne PK, Bunyak F, Hofmann AC, Lim RR, Mohan RR, Chaurasia SS, 2021. Collagen matrix perturbations in corneal stroma of Ossabaw mini pigs with type 2 diabetes. Mol. Vis 27, 666–678. http://www.molvis.org/molvis/v27/666. [PubMed: 35002212]

Soille P, 2003. Morphological Image Analysis: Principles and Applications. Springer Berlin Heidelberg, Germany. 10.1007/978-3-662-03939-7.

Sun M, Huang J, Bunyak F, Gumpper K, De G, Sermersheim M, Liu G, Lin P-H, Palaniappan K, Ma J, 2014. Superresolution microscope image reconstruction by spatiotemporal object decomposition and association: application in resolving t-tubule structure in skeletal muscle. Opt. Express 22(10), 12160–76. 10.1364/OE.22.012160. [PubMed: 24921337]

Vincent L, Soille P, 1991. Watersheds in digital spaces: an efficient algorithm based on immersion simulations. Pattern Anal. Mach. Intell. IEEE Trans. Pattern Anal. Mach. Intell 13(6), 583–98. 10.1109/34.87344.

Weis SM, Zimmerman SD, Shah M, Covell JW, Omens JH, Ross J Jr., Dalton N, Jones Y, Reed CC, Iozzo RV, McCulloch AD, 2005. A role for decorin in the remodeling of myocardial infarction. Matrix Biol. 24(4), 313–24. 10.1016/j.matbio.2005.05.003. [PubMed: 15949932]

White TL, Lewis PN, Young RD, Kitazawa K, Inatomi T, Kinoshita S, Meek KM, 2017. Elastic microfibril distribution in the cornea: Differences between normal and keratoconic stroma. Exp. Eye Res 159, 40–48. 10.1016/j.exer.2017.03.002. [PubMed: 28315339]

Wilson SE, Marino GK, Torricelli AAM, Medeiros CS, 2017. Injury and defective regeneration of the epithelial basement membrane in corneal fibrosis: A paradigm for fibrosis in other organs? Matrix Biol. 64, 17–26. 10.1016/j.matbio.2017.06.003. [PubMed: 28625845]

Highlights

- Decorin plays a functional role in the maintenance of corneal architecture.
- Decorin affects characteristic corneal collagen fibrillogenesis.
- Collagen organization, ECM assembly and its interactions with decorin during corneal wound healing.

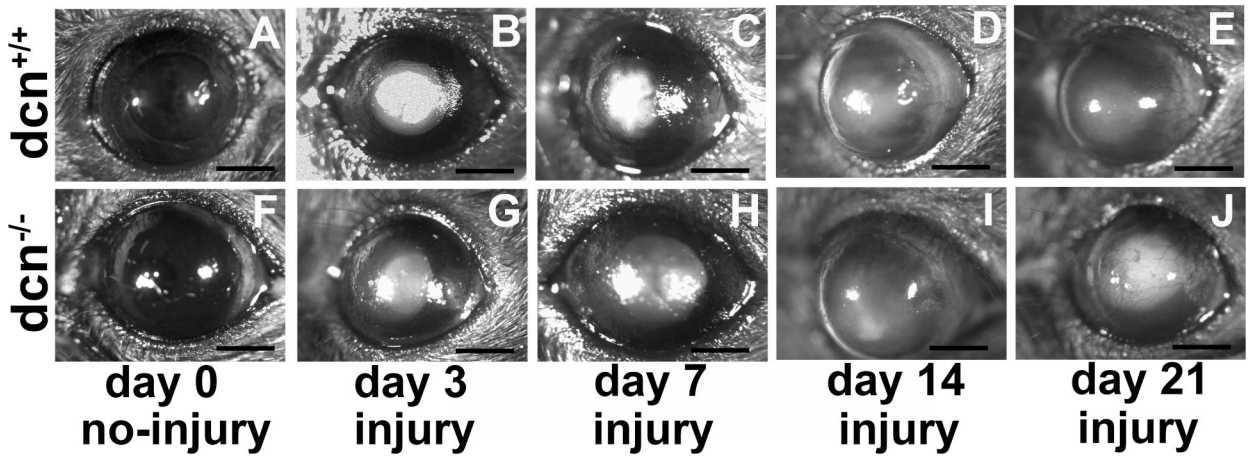

Figure 1.

Representative slit lamp biomicroscopy images showing the *dcn*$^{+/+}$ and *dcn*$^{-/-}$ corneas in +/− injury. Uninjured *dcn*$^{+/+}$ and *dcn*$^{-/-}$ corneas were clear and avascular (A & F). Conversely, alkali injured cornea showed notable haze and/or neovascularization in *dcn*$^{+/+}$ (A-E) and *dcn*$^{-/-}$ (F-J) mice at all tested times. The differences in corneal haze and neovascularization levels were more prominent in injured *dcn*$^{-/-}$ corneas (J) compared to the *dcn*$^{+/+}$ corneas (E) at day 21. These changes were not remarkably different at earlier times in injured *dcn*$^{-/-}$ (G-I) and *dcn*$^{+/+}$ (B-D) corneas. Scale bar = 1.0 mm.

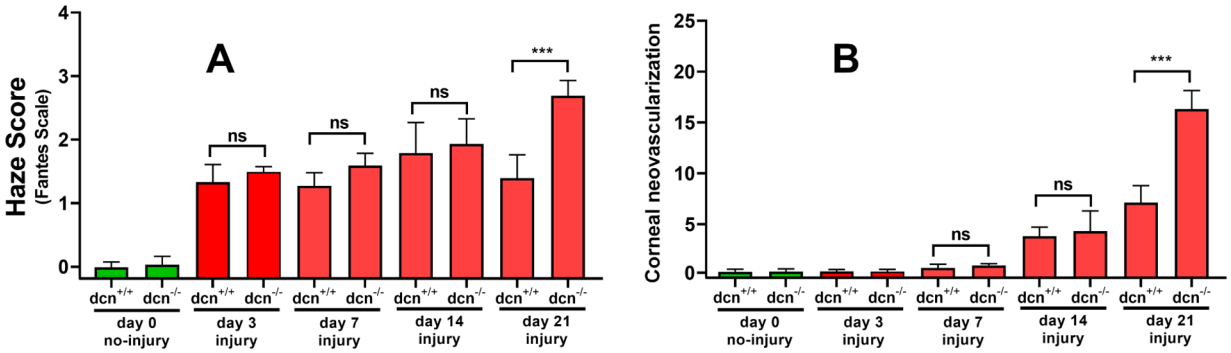

Figure 2.

Quantification of corneal haze (A) and neovascularization (B) in uninjured and injured corneas of the $dcn^{+/+}$ and $dcn^{-/-}$ mice. The corneas of no-injury groups are shown in green bars and injury groups in red bars. Injured $dcn^{-/-}$ corneas showed significantly less haze and neovascularization compared to the $dcn^{+/+}$ corneas at day 21. Although injured corneas of the $dcn^{+/+}$ and $dcn^{-/-}$ mice at earlier times (days 3, 7 and 14) exhibited clinically relevant haze and neovascularization but differences between two groups were statistically not significant. Data are expressed in ± SEM and $^{***}P < 0.001$.

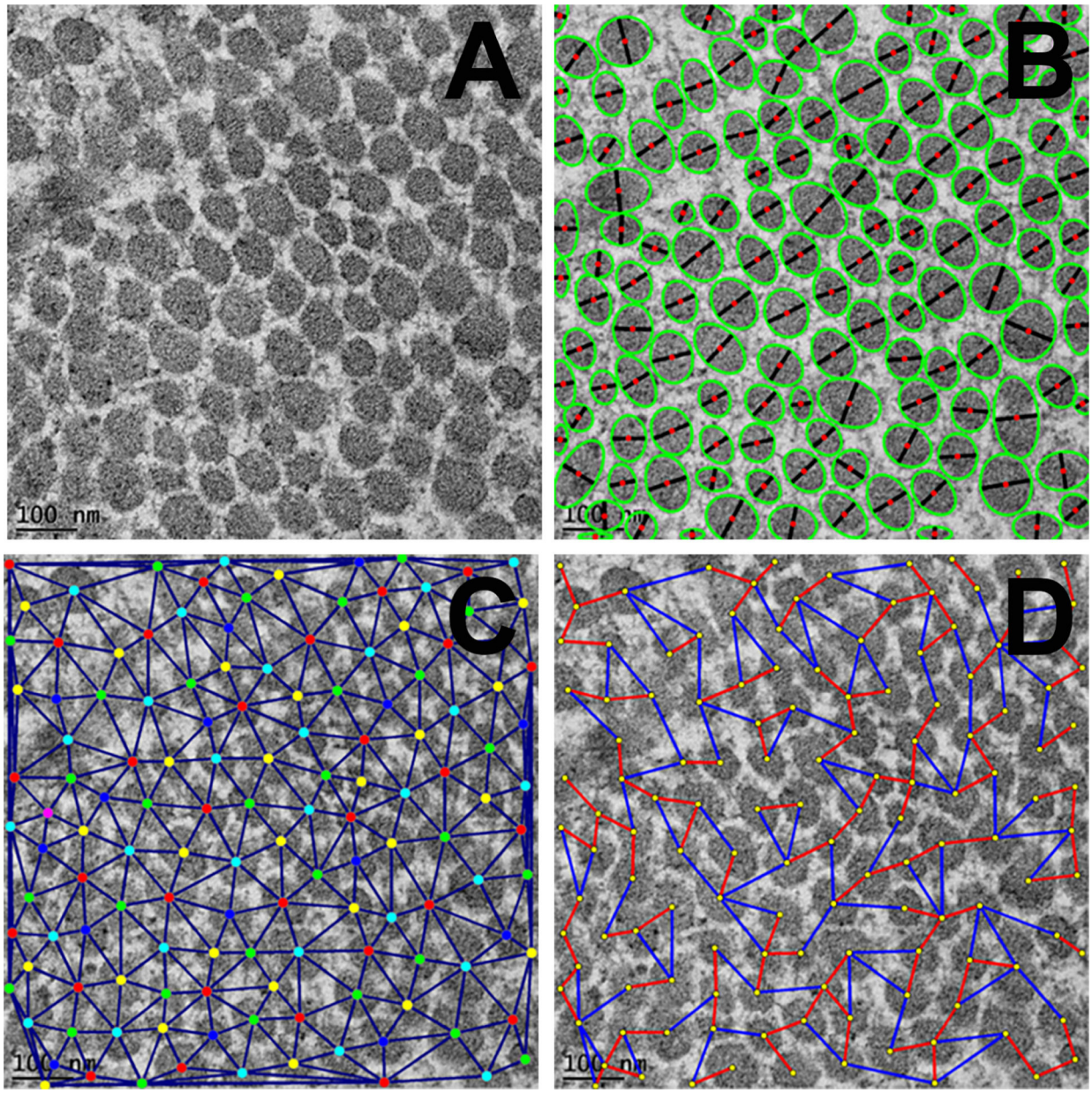

Figure 3.

Representative TEM images of corneal tissue sections showing arrangement and pattern of fibrils in cross-sections at 25,000X magnification. A: unprocessed TEM image; B: processed TEM image showing segmentation for collagen fibrils (green: ellipses fitted to individual blobs (bead like structure), black: ellipse minor axes, red: blob centroids); C: processed TEM image showing fibril centroids and neighborhood and D: processed TEM image showing nearest (red) and farthest (blue) inter fibril distances (IFD). Scale bar = 100 nm.

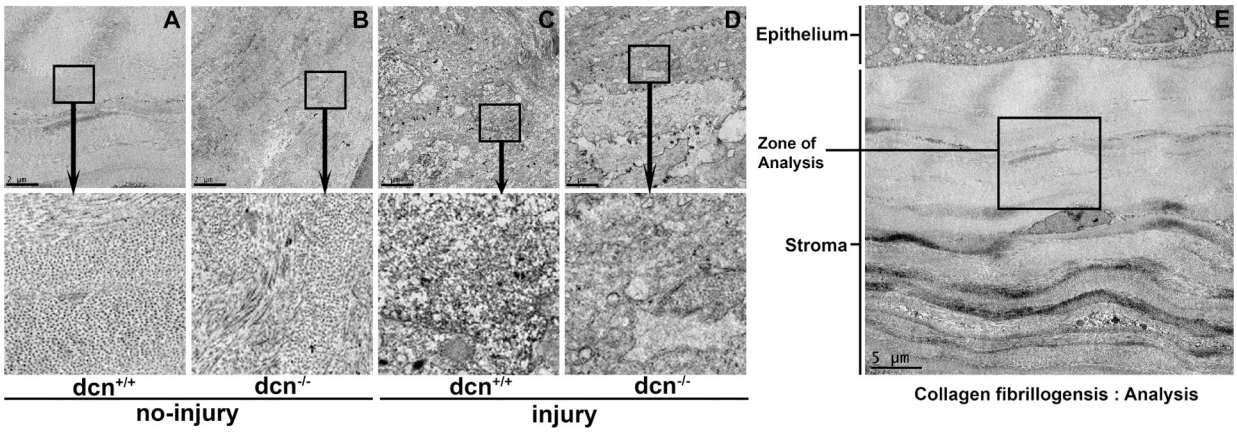

Figure 4.

The TEM images taken from ultrathin sections of no-injury and post-injury corneas of the *dcn*$^{+/+}$ and *dcn*$^{-/-}$ mice at 1500X magnification at day 21. The TEM image (4E; 500X magnification) showing "zone of analysis" in stroma chosen for ultrastructural investigation. Injured *dcn*$^{+/+}$ (C) and *dcn*$^{-/-}$ (D) corneas showed notable disruptions in fibril distribution, organization, and packing in stroma compared to the corresponding no-injury corneas (A & B). The insets show magnified view of selected area. Scale bar = 2 μm (A-D) and 5 μm (E).

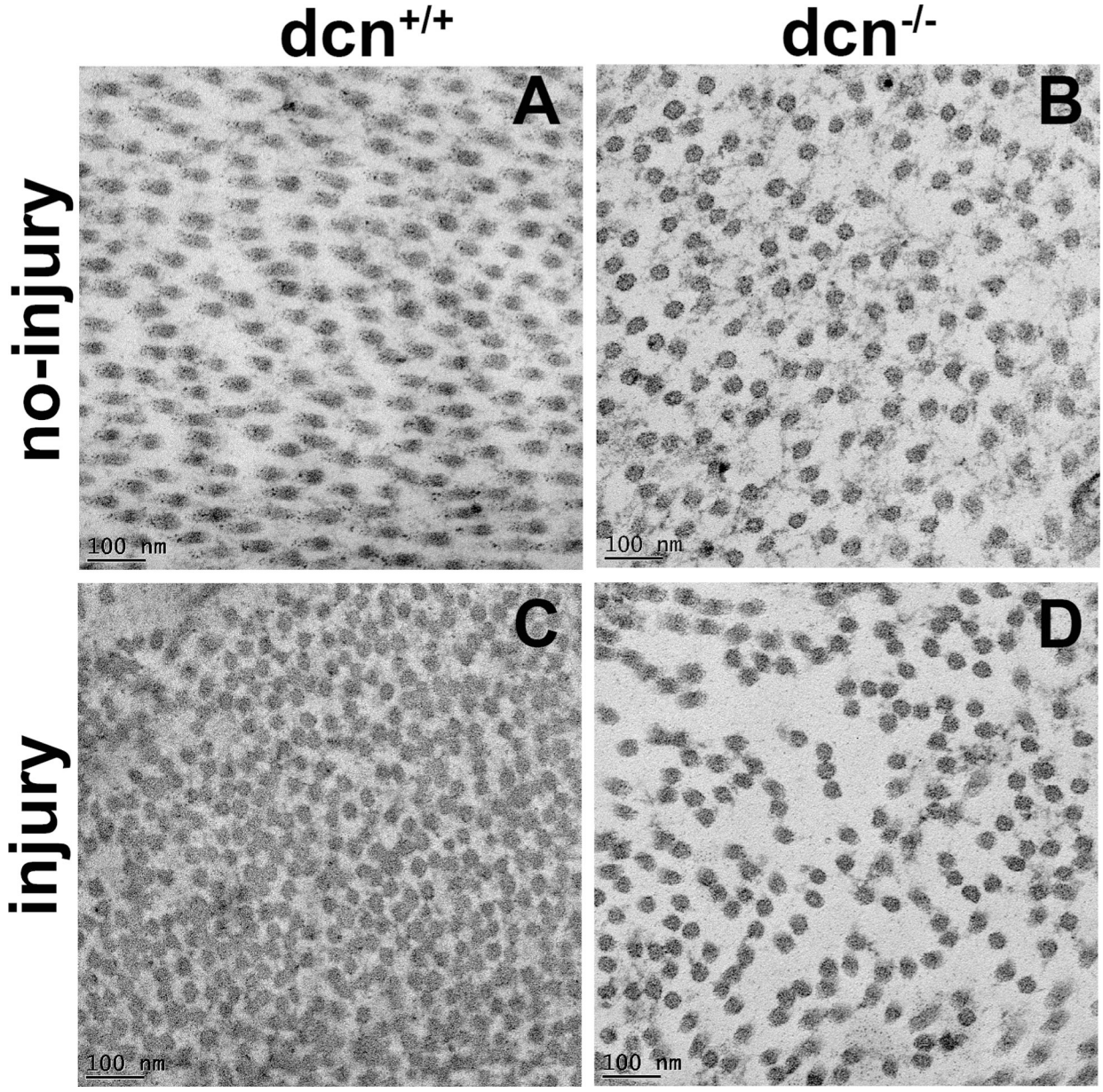

Figure 5.

Representative TEM images of no-injury and post-injury corneas of the *dcn*$^{+/+}$ and *dcn*$^{-/-}$ mice at 25,000X magnification at day 21. Substantially disorganized fibril size and arrangement pattern were observed in injured *dcn*$^{+/+}$ (C) and *dcn*$^{-/-}$ (D) corneas compared to the corresponding no-injury corneas (A & B). Scale bar = 100 nm.

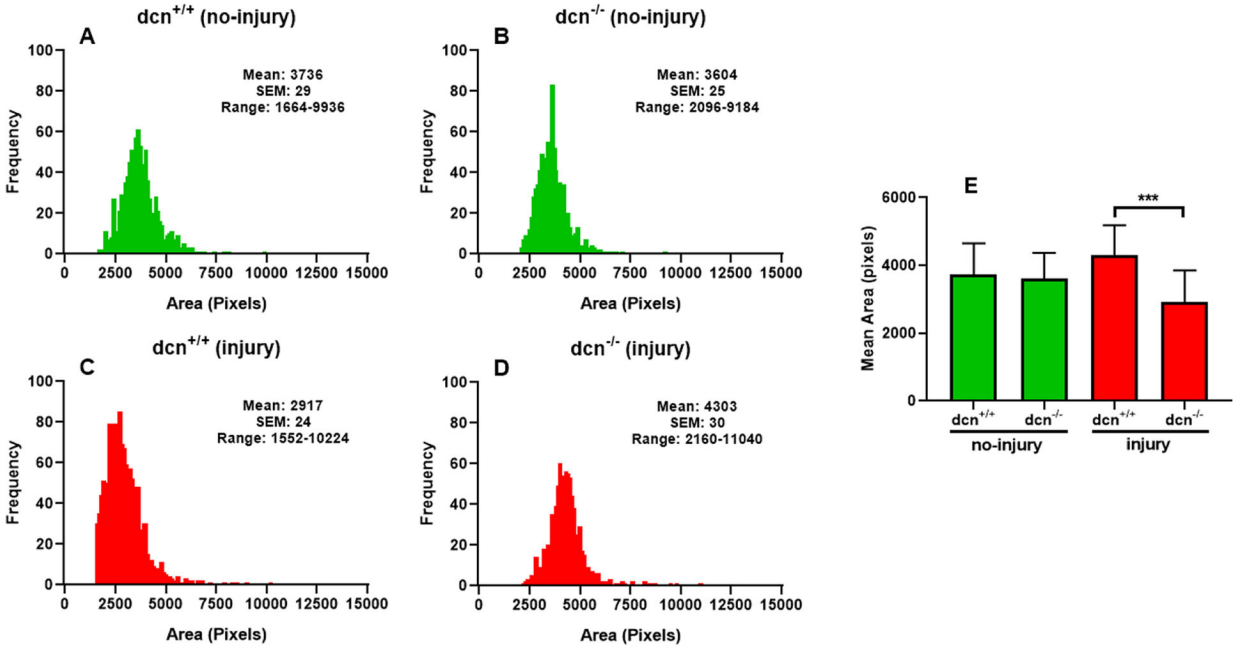

Figure 6.

Histogram showing the changes in area of fibrils at day 21 in no-injury and post-injury *dcn*$^{+/+}$ and *dcn*$^{-/-}$ mouse corneas. A vividly enhanced uneven distribution of fibrils was noted in *dcn*$^{-/-}$ corneas (D) compared to *dcn*$^{+/+}$ corneas (C) after injury. The corresponding no-injury corneas (A & B) did not show such abnormality. Quantification found changes were significant between *dcn*$^{-/-}$ and *dcn*$^{+/+}$ corneas post injury (E). Data are expressed in ± SEM and ***$P < 0.001$.

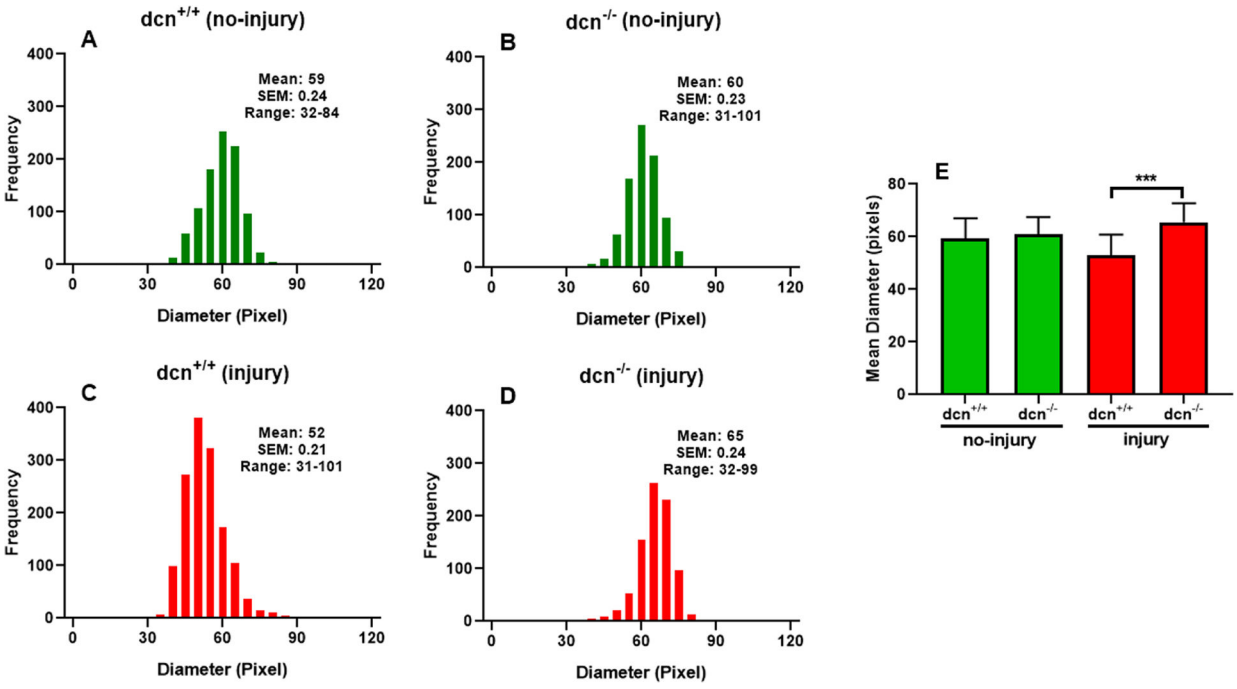

Figure 7.

Histogram showing the changes in the diameter of collagen fibrils at day 21 in no-injury and post-injury *dcn*$^{+/+}$ and *dcn*$^{-/-}$ mouse corneas. Injured *dcn*$^{-/-}$ corneas (D) showed striking changes in collagen fibril diameter compared to the *dcn*$^{+/+}$ corneas (C) after injury. Quantification found changes were significant between *dcn*$^{-/-}$ and *dcn*$^{+/+}$ corneas post injury (E). Data were expressed in ±SEM and ***$P < 0.001$.

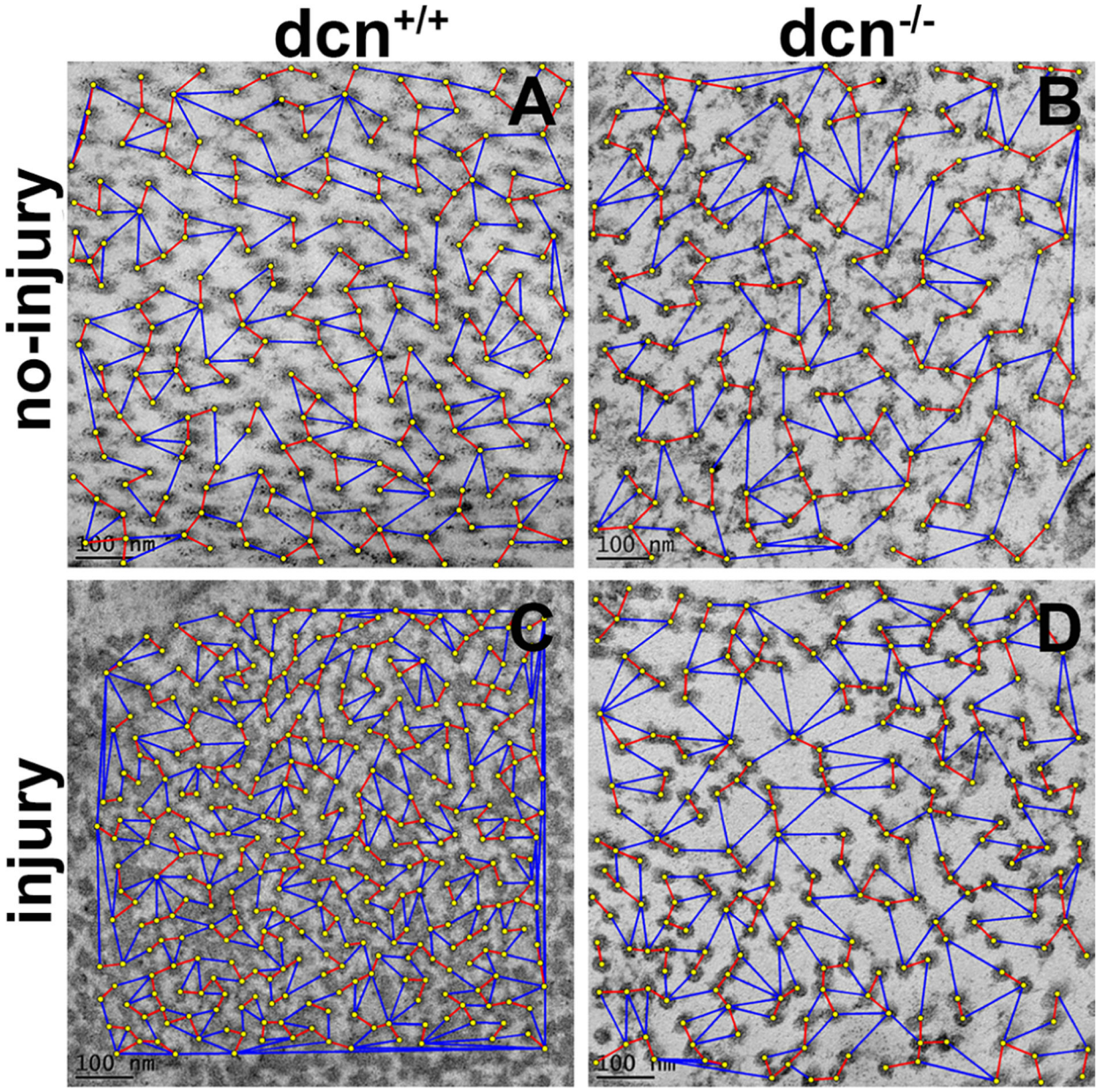

Figure 8.

Representative TEM images showing organization and distribution pattern of fibrils in stroma at day 21 in no-injury and post-injury *dcn*$^{+/+}$ and *dcn*$^{-/-}$ mouse corneas. The minimum IFD is shown by red lines and maximum IFD by blue lines. Injured *dcn*$^{-/-}$ corneas (D) showed largest minimum and maximum IFDs compared to the *dcn*$^{+/+}$ corneas (C). Uninjured *dcn*$^{+/+}$ (A) and *dcn*$^{-/-}$ (B) corneas showed unremarkable changes in IFDs. Scale bar = 100 nm.

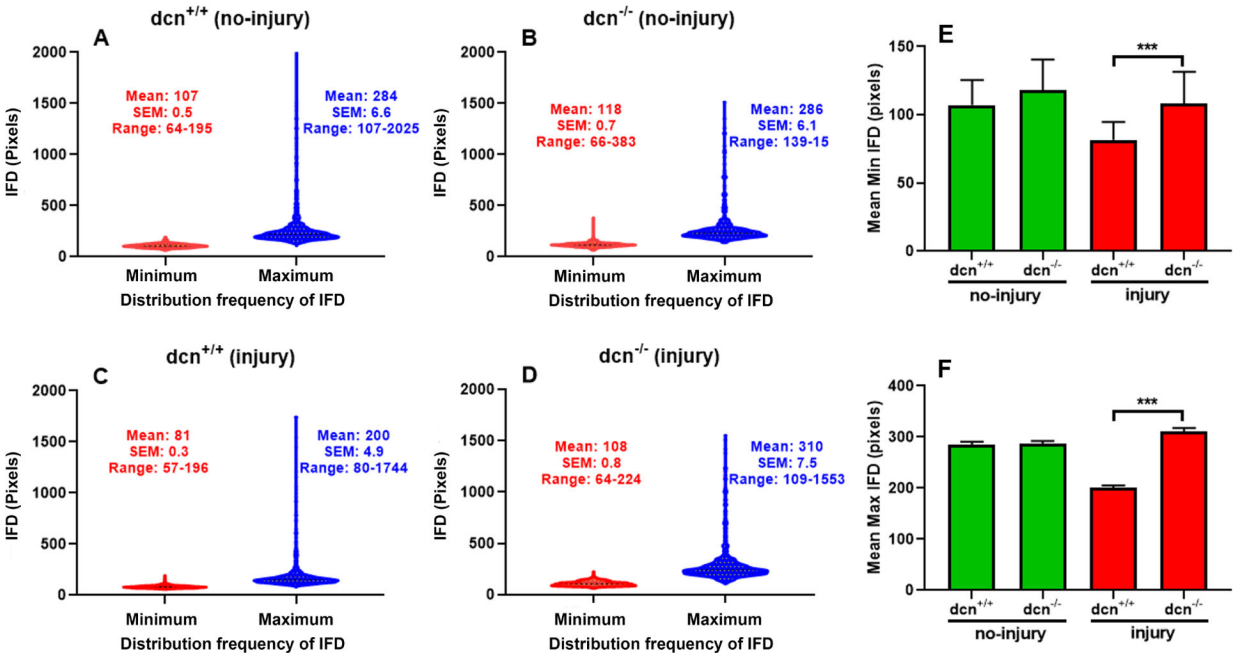

Figure 9.

Violin graphs show inter fibril distances (IFD) and distribution frequency of IFD in stroma at day 21 in no-injury and post-injury *dcn*$^{+/+}$ and *dcn*$^{-/-}$ mouse corneas. In violin graphs, minimum IFD is drawn in red color while maximum IFD in blue color. Injured *dcn*$^{-/-}$ corneas (D) showed prominent differences in minimum/maximum IFDs and its distribution frequency compared to the *dcn*$^{+/+}$ corneas (C). These differences were unremarkable in uninjured *dcn*$^{+/+}$ (A) and *dcn*$^{-/-}$ (B) corneas. Quantification found minimum (E) and maximum (F) IFDs significantly different in *dcn*$^{-/-}$ compared to the *dcn*$^{+/+}$ corneas post injury. Data were expressed in ± SEM and ***$P < 0.001$.

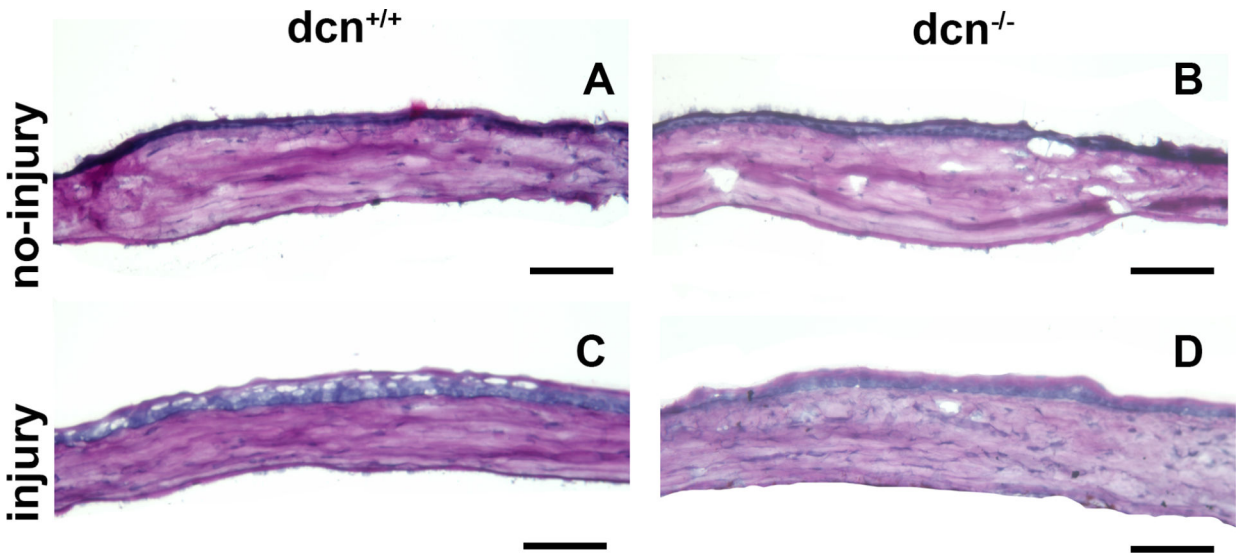

Figure 10.

Representative PAS histology images of no-injury and post-injury *dcn*$^{+/+}$ and *dcn*$^{-/-}$ mouse corneas at day 21. Injured *dcn*$^{-/-}$ (D) and *dcn*$^{+/+}$ corneas (C) showed many morphologic alterations in tissue sections, which were unremarkable in uninjured *dcn*$^{+/+}$ (A) and *dcn*$^{-/-}$ (B) corneas. Scale bar = 100 μm.

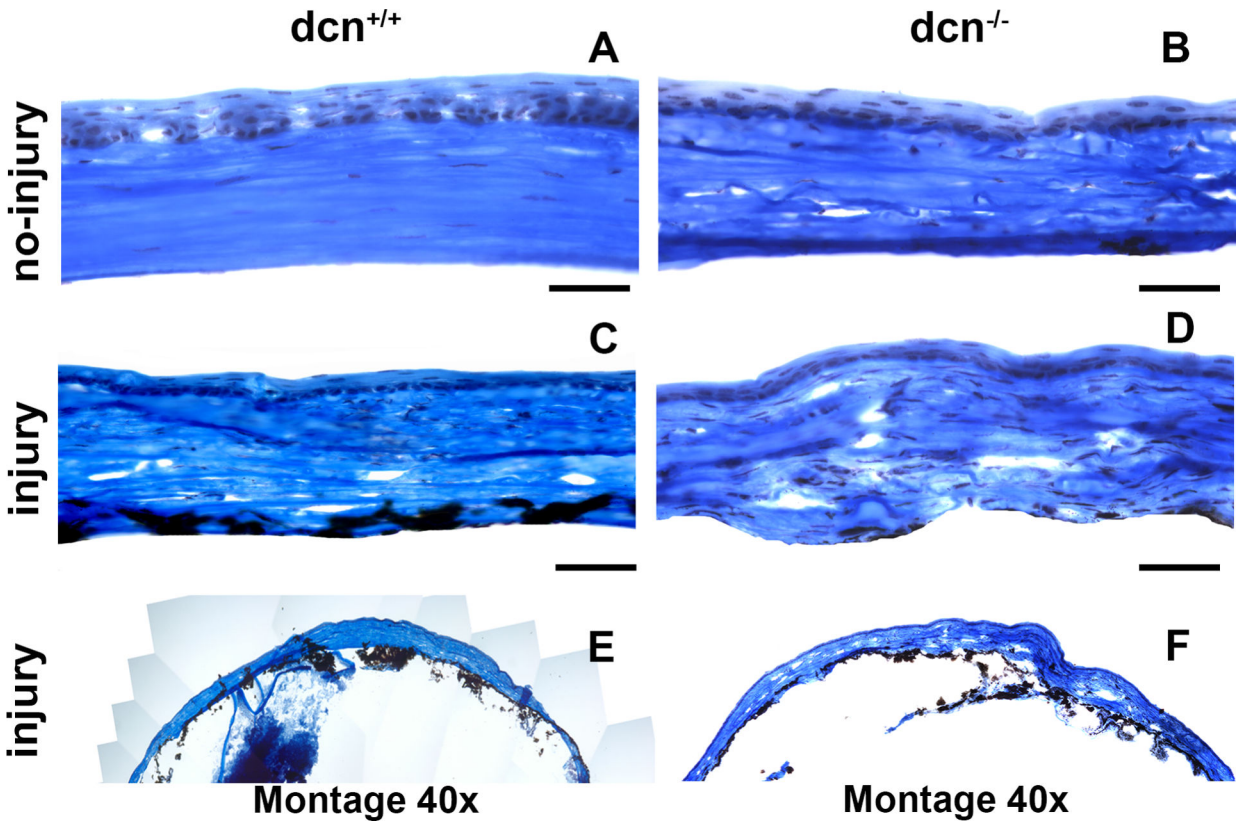

Figure 11.

Representative Masson's Trichrome histology images of no-injury and post-injury *dcn*$^{+/+}$ and *dcn*$^{-/-}$ mouse corneas at day 21. Injured *dcn*$^{-/-}$ (D) and *dcn*$^{+/+}$ corneas (C) exhibited notable differences in morphological details and collagen levels compared to the corresponding no-injury corneas (A & B). Montages created using 40X images show these effects on entire cornea of the injured *dcn*$^{+/+}$ (E) and *dcn*$^{-/-}$ (F) animals. Scale bar = 100 μm.

Table 1

List of primers used for confirmation of genotypes of mice strains

Alleles	Sequence
decorin (*dcn*), shared ($dcn^{+/-}$)	forward: 5'-ccttctggcacaagtctcttgg
decorin wild type, ($dcn^{+/+}$)	reverse: 5'-tcgaagatgacactggcatcgg
decorin null, ($dcn^{-/-}$)	reverse: 5'-tggatgtggaatgtgtgcgag

Table 2

Possible orientation patterns based on the value of eigenvalues λ_1 and λ_2 of the Hessian matrix ($I\lambda_1 I \geq I\lambda_2 I$) (Frangi et al., 1998).

λ_1	λ_2	Orientation Pattern
Low	Low	Flat or Noise no preferred direction
High−	Low	Bright tubular structure
High+	Low	Dark tubular structure
High−	High−	Bright blob-like structure
High+	High+	Dark blob-like structure